Atmospheric
Chemistry
and Physics

Retrieving tropospheric NO$_2$ vertical column densities around the city of Beijing and estimating NO$_x$ emissions based on car MAX-DOAS measurements

Xinghong Cheng[1], Jianzhong Ma[1], Junli Jin[2], Junrang Guo[1], Yuelin Liu[3], Jida Peng[4], Xiaodan Ma[5], Minglong Qian[6], Qiang Xia[6], and Peng Yan[2]

[1]State Key Lab of Severe Weather & Key Laboratory for Atmospheric Chemistry, Chinese Academy of Meteorological Sciences, Beijing 100081, China
[2]CMA Meteorological Observation Centre, Beijing 100081, China
[3]College of Architecture and Environment, Sichuan University, Chengdu 610065, China
[4]Meteorological Institute of Fujian, Fuzhou 350001, China
[5]Nanjing University of Information Science and Technology, Nanjing 210044, China
[6]China National Huayun Technology Development Corporation, Beijing 100081, China

Correspondence: Xinghong Cheng (cxingh@cma.gov.cn) and Jianzhong Ma (majz@cma.gov.cn)

Abstract. We carried out 19 city-circle-around car multi-axis differential optical absorption spectroscopy (MAX-DOAS) experiments on the 6th Ring Road of Beijing in January, September, and October 2014. The tropospheric vertical column densities (VCDs) of NO$_2$ were retrieved from measured spectra by the MAX-DOAS technique and used to estimate the emissions of NO$_x$ ($\equiv$ NO + NO$_2$) from urban Beijing during the experimental periods. The offline LAPS-WRF-CMAQ model system was used to simulate the wind fields by assimilation of observational data and calculate the NO$_2$-to-NO$_x$ concentration ratios, both of which are also needed for the estimation of NO$_x$ emissions. The NO$_x$ emissions in urban Beijing for the different months derived from the car MAX-DOAS measurements in this study were compared to the multi-resolution emission inventory in China for 2012 (MEIC 2012). Our car MAX-DOAS measurements showed higher NO$_2$ VCD in January than in the other two months. The wind field had obvious impacts on the spatial distribution of NO$_2$ VCD, with the mean NO$_2$ VCD along the 6th Ring Road typically being higher under the southerly wind than under the northerly wind. In addition to the seasonal difference, the journey-to-journey variations of estimated NO$_x$ emission rates (E_{NO_x}) were large even within the same month, mainly due to uncertainties in the calculations of wind speed, the ratio of NO$_2$ and NO$_x$ con-

centration, and the decay rate of NO$_x$ from the emission sources to the measured positions under different meteorological conditions. The ranges of E_{NO_x} during the heating and non-heating periods were 22.6×10^{25} to 31.3×10^{25} and 9.6×10^{25} to 12.0×10^{25} molec. s^{-1}, respectively. The average E_{NO_x} values in the heating and non-heating periods were $26.9 \pm 6.1 \times 10^{25}$ molec. s^{-1} and $11.0 \pm 1.2 \times 10^{25}$ molec. s^{-1}, respectively. The uncertainty range of E_{NO_x} was 20 %–52 %. The monthly emission rates from MEIC 2012 are found to be lower than the estimated E_{NO_x}, particularly in January. Our results provide important information and datasets for the validation of satellite products and also show how car MAX-DOAS measurements can be used effectively for dynamic monitoring and updating of the NO$_x$ emissions from megacities such as Beijing.

1 Introduction

Over the past decade, serious haze events have occurred frequently in fall and winter in Beijing due to massive anthropogenic emissions from the combustion of fossil fuels and other sources (He et al., 2013; Zhang et al., 2013). High concentrations of aerosol particulate matter with dynamic diam-

eters less than 2.5 μm (PM$_{2.5}$) threaten public health (Cao et al., 2014), disturb traffic operation by affecting visibility, and result in perturbations to the weather and climate by scattering and absorption of solar radiation (Liao et al., 2015; Cheng et al., 2017). Measurements have shown that organic matter (OM), sulfate, nitrate, and ammonium made up more than 78 % of the PM$_{2.5}$ in Beijing during January 2013 (Huang et al., 2014). Fractions of nitrate in PM$_{2.5}$ have increased recently with the control of industry and coal in the Beijing–Tianjin–Hebei region, which has reduced SO$_2$ emissions and the ratio of sulfate in PM$_{2.5}$, while traffic emissions are still at high levels. A recent study based on the aerosol observations at the campus of Peking University in 2014 revealed that aerosol pollution is nitrate-driven in spring and early fall and OM-driven in late fall and winter (Tan et al., 2018). The study suggested that nitrate formation was more significant than sulfate formation during severe pollution episodes in Beijing. Therefore, studies on the spatiotemporal variation of NO and NO$_2$ (together denoted as NO$_x$), with the latter being a precursor of nitrate aerosols, are very important for understanding the aerosol formation and its influencing factors.

Emission inventories are usually developed by the so-called bottom-up approach, which is based on combinations of activity statistics (such as energy consumption and industrial production) and source- or region-specific emission factors (Hao et al., 2002; Zhang et al., 2007; Zhao et al., 2012; Streets et al., 2013). However, there are large uncertainties in bottom-up emission inventories associated with the statistics, emission factors, temporal allocation profiles, and grid allocation factors (Ma and Van Aardenne, 2004; Zhao et al., 2012). Moreover, estimating "current" emissions by the bottom-up methodology is fundamentally difficult because publication of basic statistics is generally a couple of years behind. The "top-down" emission estimate is a useful supplement to bottom-up estimates, which are subject to uncertainties in emission factors and emission activities (Streets et al., 2013). Inverse modeling, in which emissions are optimized to reduce the differences between simulated and observed data, is a powerful method that solves the problems of the bottom-up approach. Recently, its application to the estimation of NO$_x$ emissions has been widely reported. NO$_x$ emission rates are derived by constraining satellite observations using the relationship between model-simulated NO$_2$ vertical column density (VCD) and primary NO$_x$ emission estimates from the bottom-up approach (Martin, 2002; Jaeglé et al., 2005; Konovalov et al., 2006; Wang et al., 2007; Lin et al., 2012; Zyrichidou et al., 2015). Nevertheless, errors and uncertainties still exist in the retrieval of satellite data, which leads to a large decrease in the accuracy of estimated emissions, particularly in highly polluted regions such as Beijing and its surroundings (Ma et al., 2013a; Jin et al., 2016). Uncertainties can arise from noise, surface albedo, cloud blocks, profile shape, interference from ozone absorption, correlations with other retrieved parameters, fitting wavelength win-

dow, and so forth (Jin et al., 2016; Ma et al., 2013a; Shaiganfar et al., 2011, 2017). Air mass factor (AMF) errors can produce additional errors during the conversion process from the slant to vertical columns. Therefore, comprehensive ground-based measurements of the tropospheric columns and vertical profiles of NO$_2$ are quite important and necessary to evaluate and validate satellite retrieval products.

Multi-axis differential optical absorption spectroscopy (MAX-DOAS) is a ground-based remote-sensing technique developed during the last 2 decades. It makes use of the scattered sunlight measured from the horizontal through zenith-pointing directions to retrieve the VCD and vertical profiles of trace gases and aerosols with relatively high sensitivity in the lower atmosphere (Hönninger et al., 2004; Wagner et al., 2004; Platt and Stutz, 2008). MAX-DOAS has been extensively used to derive tropospheric column information of NO$_2$ and some other pollutants in various regions (Wittrock et al., 2004; Brinksma, et al., 2008; Irie et al., 2008; Vlemmix et al., 2010; Li et al., 2013; Hendrick et al., 2014; Tan et al., 2008; Wagner et al.,2011). Mobile (or car) MAX-DOAS measurements have been used to quantify NO$_x$ emissions from cities and regions such as Beijing (Johansson et al., 2008), Mexico (Johansson et al., 2009), Mannheim and Ludwigshafen (Ibrahim et al., 2010), Delhi (Shaiganfar et al., 2011), Shanghai (Wang et al., 2012), and North China (Wu et al., 2018). Compared to ground-based observations at a fixed site, car MAX-DOAS measurements can provide information on the horizontal spatial distribution of pollutants, which is important for explaining the urban/regional representativeness of satellite observations and validating the NO$_2$ VCDs and NO$_x$ emission estimates from the new, high pixel resolution measurements by the TROPOMI instrument on Sentinel-5P over megacities such as Beijing. Moreover, due to the rapid expansion of urban areas and increasing energy consumption, both locations and strength of emission sources in Beijing might have changed significantly. Therefore, intensive car MAX-DOAS measurement campaigns are still needed to estimate the emissions of NO$_x$ in Beijing. Mean wind speed and wind direction along the ring road during the sampling periods were usually used to estimate NO$_x$ emissions in previous studies. Since the wind field changes rapidly due to local circulation and then results in uncertainties in quantification of NO$_x$ emissions (Johansson et al., 2008; Shaiganfar et al., 2011, 2017; Davis et al., 2019), refined and accurate simulations of wind fields are needed for the exact emission estimate.

In this study, we estimated the total NO$_x$ emissions from urban Beijing based on the VCD of NO$_2$ obtained from intensive car MAX-DOAS measurements on the 6th Ring Road of Beijing in January, September, and October 2014. The offline LAPS-WRF-CMAQ model system with the data assimilation method was used to derive wind speed, wind direction, and NO$_2$/NO$_x$ concentration ratios, which are needed to estimate total urban NO$_x$ emissions based on car MAX-DOAS measurements. We attempted to accurately estimate the NO$_x$
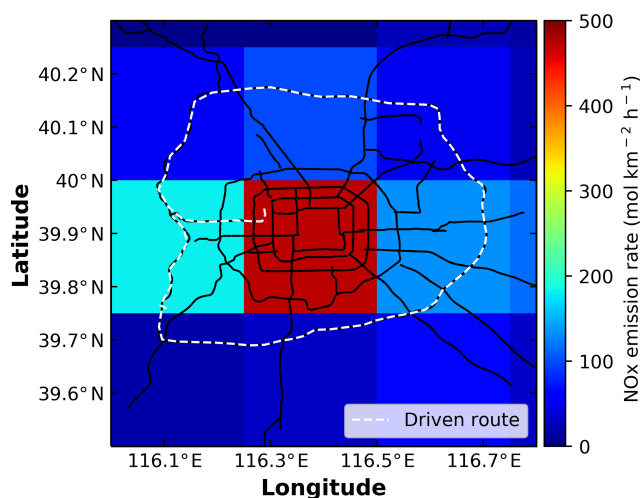
Figure 1. Driving routes (white dashed line) of the car MAX-DOAS experiment on the 6th Ring Rd of Beijing and distribution of yearly averaged NO$_x$ emission rate (mol km^{-2} h^{-1}) from the MEIC 2012.

emission rates and the seasonal difference and deeply investigate the uncertainties and appropriate meteorological conditions for the estimation based on car MAX-DOAS measurements. This paper is organized as follows: Sect. 2 describes the intensive car MAX-DOAS experiments and the retrieval method for deriving tropospheric NO$_2$ VCD, the model system used to simulate the wind fields and the ratios of NO$_2$ and NO$_x$, and the method used to quantify total NO$_x$ emissions. Section 3 presents the results of the NO$_2$ VCD and the estimated NO$_x$ emissions as well as their uncertainties due to simulated errors in the wind field. Conclusions are provided in Sect. 4.

2 Theory, experimental, and method

2.1 Formula to estimate urban NO$_x$ emissions

The complete NO$_2$ flux F_{NO_2} across the urban Beijing area encircled by the driving route S is estimated according to the closed integral method (CIM) of Ibrahim et al. (2010).

$$F_{NO_2} = \oint_s VCD_{NO_2}(s) \cdot \boldsymbol{w} \cdot \boldsymbol{n} \cdot ds \tag{1}$$

Here $VCD_{NO_2}(s)$ is the NO$_2$ VCD at the sampling position within the driving route; $\boldsymbol{n}$ indicates the normal vector parallel to the Earth's surface and orthogonal to the driving direction at the position of the driving route; $\boldsymbol{w}$ is the average wind vector within the NO$_2$ layer. We carried out car MAX-DOAS measurements along closed driving routes around large emission sources, i.e., the 6th Ring Road of Beijing (Fig. 1).

We averaged the wind vector data from the Weather Research and Forecasting (WRF) model between surface and

1000 m altitude weighted by the winter exponentially decreasing profiles according to the method of Shaiganfar et al. (2017).

$$\boldsymbol{w} = \frac{\sum_i w(z_i) \cdot e^{-\frac{z_i}{z_0}}}{\sum_i e^{-\frac{z_i}{z_0}}} \tag{2}$$

Here $w(z_i)$ is the wind vector at altitude z_i and z_0 indicates the assumed scale height of 300 m for winter.

According to the CIM, the complete NO$_x$ emissions from the encircled areas are determined considering the partitioning between NO and NO$_2$ (c_L) and the finite lifetime of NO$_x$ (c_τ).

$$E_{NO_x} = c_L \cdot c_\tau \cdot F_{NO_2} \tag{3}$$

$$c_L = \frac{C_{NO_x}}{C_{NO_2}} \tag{4}$$

Here c_L is simply the ratio of NO$_x$ (C_{NO_x}) and NO$_2$ (C_{NO_2}) bulk concentration in the polluted layer, which are simulated by the Community Multiscale Air Quality Modeling System (CMAQ) model in this study. It is a function of the Leighton ratio ($L_c = [NO] / [NO_2]$), $c_L = 1 + L_c$. To analyze whether there is the impact of VOCs on lifetime of NO$_x$ or not, we also calculate another Leighton ratios, L_r, referring to the method of Davis et al. (2019).

$$L_r = \frac{j_{NO_2}[NO_2]}{k_8 [NO][O_3]}, \tag{5}$$

where j_{NO_2} is the NO$_2$ photolysis rate and k_8 is the temperature-dependent rate constant for the reaction between NO and O$_3$. We calculate j_{NO_2} according to the method of Dickerson et al. (1982).

c_τ describes the decay of NO$_x$ from the emission sources to measured positions. c_τ can be estimated from the NO$_x$ lifetime τ, which is the reciprocal of the product of reaction rate constant k, OH concentration (C_{OH}) and air density (M) (Ma et al., 2013b), and transport time t, which is the distance between emission source and sampling position, r, divided by the wind speed $\boldsymbol{w}$.

$$c_\tau = e^{\frac{t}{\tau}} = e^{\frac{r/\boldsymbol{w}}{\tau}} \tag{6}$$

$$\tau = \frac{1}{k \cdot C_{OH} \cdot M} \tag{7}$$

We firstly calculated averaged simulated wind speed and direction, the ratio of NO$_x$ and NO$_2$, and the NO$_x$ lifetime from surface to 1000 m at every sampling position on the 6th Ring Rd of Beijing for each journey and computed the distance between the sampling position and the center of Beijing for r. Then, we computed c_τ, F_{NO_2}, and E_{NO_x}. The lifetime τ was calculated with the simulated average OH concentration and air density from surface to 1000 m at each sampling position for each journey.

2.2 Car MAX-DOAS measurements

2.2.1 Instrument and experiment

We measured and retrieved tropospheric NO$_2$ VCD along the sixth ring road of Beijing (hereafter referred to as 6th Ring Rd) in January, September, and October 2014 using a Mini MAX-DOAS instrument mounted on the vehicle.

The instrument, manufactured at Hoffmann Messtechnik GmbH, Germany, is a fully automated, light-weight spectrometer designed for the spectral analysis of scattered sunlight by the MAX-DOAS technique (Hönninger et al., 2004; Davis et al., 2019). The same type of instrument was used in previous studies, including long-term site measurements in Beijing (Ma et al., 2013a) and a car MAX-DOAS observational journey in Europe (Wagner et al., 2010a). The instrument consists of a hermetically sealed metal box of approximately 3 L volume containing entrance optics, a fiber-coupled spectrograph, and all electronics. A spectrometer with the Ocean Optics USB2000+ model is used. A stepper motor, adjusted outside the box, rotates the whole instrument to control the elevation viewing angle. The spectrograph covers the range 292–436 nm and its entrance slit is 50 μm wide. A Sony ILX511 CCD (charged coupled device) detects the light in 2048 individual pixels. The whole spectrograph is cooled by a Peltier stage to guarantee a stable temperature of the optical setup and a small dark current signal. For this study, the instrument was mounted on the roof of a car. Inside the car, two 12 V DC batteries alternatively supplied electronic power for the running of instruments and a laptop computer, with a script run by the DOASIS software (Kraus, 2001) to control the measurement process and the recording of spectra. The temperature of the spectrograph was set to be maintained at $-5\,°C$ in January and at $0\,°C$ in September and October, well below the ambient temperatures during the experimental days of the study. The signal spectra of dark current and electronic offset were measured each day before and after the field experiment on the road, with 10 000 ms and 1 scan for dark current measurements and 3 ms and 1000 scans for electronic offset measurements. Measurements were made alternatively at 30 and 90° elevation angles, with every 30° measurement immediately followed by a 90° measurement. Each elevation angle measurement had an integration time of about 1 min, including typically 300–400 scans for an average spectrum.

The instrument onboard the car was operated to measure scattered sunlight from the driving forward direction. There were no high buildings on both sides of the 6th Ring Rd, and the measurements were made at a wide-field view. The driving speed was typically controlled at 80–90 km h^{-1}, and it generally took about 2.0–2.5 h to complete one circle (about 187 km) around the 6th Ring Rd. Figure 1 shows the driving route of the car MAX-DOAS experiment on a map of Beijing and spatial distribution of the yearly NO$_x$ emission rate with a resolution of 0.25° × 0.25° from the MEIC inventory in 2012, which includes the transportation, power plant, residential, industry, and agriculture sectors. For this study, the field experiments were carried out on 14 selected days, with one or two circling journeys each day. In total, there are 19 circling journeys available. The sampling periods in this experiment and the meteorological conditions are listed in Table 1. The average wind speeds for experimental days in January, September, and October were 2.5, 2.5, and 2.4 m s^{-1}, the corresponding total cloud fractions were 4.9, 7.5, and 4.2, and the mean planetary boundary layer (PBL) heights were 192, 188, and 238 m, respectively. The dominant wind directions in the three months were much more variable, including the northerly, southerly, and other directions and static wind. Since variations of the wind field can affect the estimation of E_{NO_x}, we synthetically analyze the distribution of the wind field using simulations from the WRF model and reanalysis data with a spatial resolution of 0.125° × 0.125° every 3 h from the European Centre for Medium-Range Weather Forecasts (ECMWF). In some cases, the wind direction changed slightly within one circling journey period, which is marked as southerly (S) or northerly (N) type in Table 1. However, the wind field during some journeys was convergent or divergent in some areas of Beijing, which is marked as other type (O), and the wind speed was very low in three journeys, which is marked as static type (St). To estimate the NO$_x$ emissions accurately using the CIM, the wind speed needs to be sufficiently high, so that the transport across the encircled area is fast compared to the atmospheric lifetime of the trace gas (Ibrahim et al., 2010). In this study, we only consider the circling journeys with a consistent wind field (S or N type) and relatively high wind speed to estimate the NO$_x$ emissions. The related information for all the journeys, including 11 selected ones for emission estimation, is given in Table 1.

2.2.2 Spectral retrieval

The retrieval of NO$_2$ slant column densities (SCDs) is based on the DOAS method (Platt, 1994). The WinDOAS software (Fayt and Van Roozendael, 2011) was adopted to analyze the spectra in the 400–431 nm range on a daily basis. The Fraunhofer reference spectrum (FRS) was selected among the measured spectra at the 90° elevation angle each day by two steps: first, a spectrum measured around noon was chosen; second, the spectrum corresponding to the minimum NO$_2$ SCD derived in the preliminary analysis using the FRS from the first step was finally selected. The absorption cross sections of NO$_2$ at 294 K (Vandaele et al., 1998), O$_3$ at 221 K (Burrows et al., 1999), and the oxygen dimer O$_4$ at 298 K (Greenblatt et al., 1990), as well as a FRS, a Ring spectrum calculated from the FRS by DOASIS (Kraus, 2001), and a polynomial of third order were included in the spectral fitting process. Figure 2 shows an example of our spectral analysis for a measurement on 18 January 2014, 11:39:38 BJT. As

Table 1. Sampling periods of the car MAX-DOAS experiment and corresponding meteorological conditions over Beijing in January, September, and October 2014.

Journey	Date	Time (BJT)	Wind speed (m s^{-1})	Type of wind field[a]	Total cloud fraction	PBL height (m)
1	18 January 2014	10:48–13:09	2	St	0	564
2	19 January 2014	13:31–15:40	1	O	7	167
3[b]	21 January 2014	13:15–15:32	3	S	0	163
4	23 January 2014	10:39–12:25	3	O	7	187
5	23 January 2014	13:07–15:12	2	O	7	163
6[b]	24 January 2014	10:42–12:03	2	N	8	39
7[b]	24 January 2014	13:03–15:09	3	N	8	39
8[b]	26 January 2014	10:21–12:13	5	S	5	341
9	27 January 2014	09:11–11:38	2	St	7	75
10[b]	27 January 2014	13:30–15:28	2	O	0	178
11[b]	14 September 2014	09:40–12:52	4	N	10	173
12[b]	14 September 2014	15:02–17:17	2	N	10	226
13	17 September 2014	09:07–11:42	2	St	7	173
14[b]	19 September 2014	09:09–11:50	2	S	3	178
15	9 October 2014	13:04–14:44	1	St	7	43
16[b]	10 October 2014	09:52–12:28	2	S	7	663
17[b]	12 October 2014	14:02–16:42	3	N	7	167
18[b]	13 October 2014	09:12–11:59	3	N	0	186
19	13 October 2014	13:11–16:27	3	O	0	130

[a] Four types of wind field are southerly (S), northerly (N), other (O), and static (St). [b] The data are preliminarily selected to estimate the NO$_x$ emissions.

shown in the figure, the atmospheric NO$_2$ absorption structure can be clearly extracted from the measured spectra.

2.2.3 Derivation of tropospheric NO$_2$ VCD

The trace gas VCD in the troposphere can be calculated using its SCD divided by the AMF at an elevation angle, α:

$$\mathrm{VCD_{trop}} = \frac{\mathrm{SCD_{trop}}(\alpha)}{\mathrm{AMF_{trop}}(\alpha)}. \tag{8}$$

For the in situ MAX-DOAS measurements, a FRS from the same elevation sequence was used in most cases, and the stratospheric absorption can be assumed to be the same during one elevation sequence. Therefore, the VCD$_{\mathrm{trop}}$ can be calculated by extending Eqs. (8) to (9) using the so-called differential tropospheric slant column density (DSCD$_{\mathrm{trop}}(\alpha) = \mathrm{SCD_{trop}}(\alpha) - \mathrm{SCD_{trop}}(90°)$) divided by the differential air mass factor (DAMF$_{\mathrm{trop}}(\alpha) = \mathrm{AMF_{trop}}(\alpha) - \mathrm{AMF_{trop}}(90°)$):

$$\mathrm{VCD_{trop}} = \frac{\mathrm{DSCD_{trop}}(\alpha)}{\mathrm{DAMF_{trop}}(\alpha)} = \frac{\mathrm{DSCD_{meas}}(\alpha)}{\mathrm{DAMF_{trop}}(\alpha)}, \tag{9}$$

with $\mathrm{DSCD_{meas}}(\alpha) = \mathrm{SCD_{meas}}(\alpha) - \mathrm{SCD_{ref}}$ (Wagner et al., 2010b; Ma et al., 2013a).

For the car MAX-DOAS measurements, the trace gas concentrations can change significantly during one measurement sequence, and thus the dependence of retrieved trace gas

DSCDs on the elevation angle may not be so regular as for the in situ measurements. Therefore, it would be a better choice to use a single FRS for the analysis of all the spectra measured along the driving route (Wagner et al., 2010b). According to Wagner et al. (2010b), Eq. (9) can be further extended to

$$\mathrm{VCD_{trop}} = \frac{\mathrm{DSCD_{meas}}(\alpha) - \mathrm{DSCD_{offset}}(\mathrm{SZA})}{\mathrm{AMF_{trop}}(\alpha)}, \tag{10}$$

where DSCD$_{\mathrm{offset}}$ depends on the solar zenith angle (SZA) and thus local time, t_i. For each elevation sequence i during the individual measurement day, DSCD$_{\mathrm{offset}}$ is calculated from a single pair of measurements with

$$\mathrm{DSCD_{offset}}(t_i) = \frac{\begin{array}{c}\mathrm{AMF_{trop}}(90°)\cdot\mathrm{DSCD_{meas}}(\alpha, \ t_i) \\ -\mathrm{AMF_{trop}}(\alpha)\cdot\mathrm{DSCD_{meas}}(90°, t_i)\end{array}}{\mathrm{AMF_{trop}}(\alpha) - \mathrm{AMF_{trop}}(90°)}. \tag{11}$$

The time series of the calculated DSCD$_{\mathrm{offset}}(t_i)$ in this study could be fitted by a low-order polynomial, e.g., $P(x) = a_0 + a_1 \cdot x + a_2 \cdot x^2$, as a function of time. The fitted polynomial then represents the best guess for DSCD$_{\mathrm{offset}}$ and can be used to calculate the VCD$_{\mathrm{trop}}$ from Eq. (10). In this study, the AMF was calculated by the geometric approximation (Brinksma et al., 2008; Wagner et al., 2010b), that is,

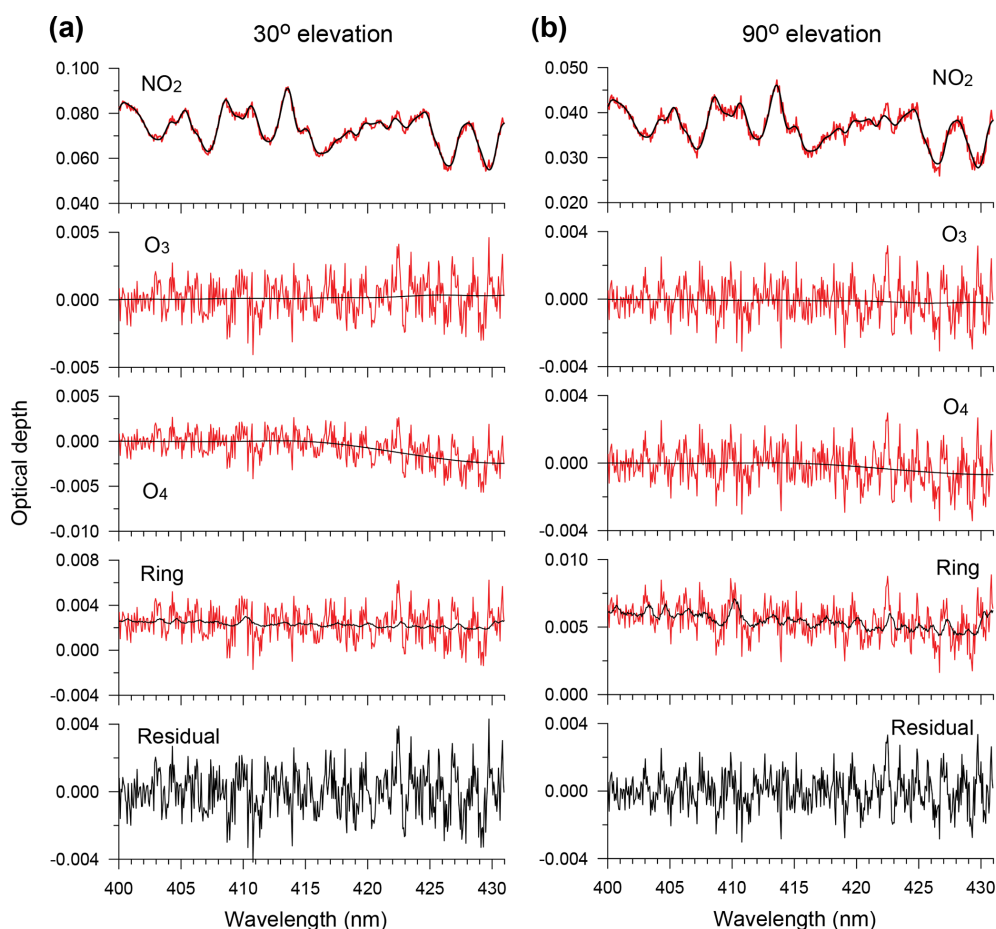$$\mathrm{AMF_{trop}}(\alpha) \approx \frac{1}{\sin(\alpha)}. \tag{12}$$

Figure 2. Examples of the NO$_2$ retrieval from two successive spectra measured **(a)** at a 30° elevation angle (with NO$_2$ differential slant column density (DSCD) of 1.2×10^{17} molec. cm^{-2}) and **(b)** at a 90° elevation angle (with NO$_2$ DSCD of 6.2×10^{16} molec. cm^{-2}) on 18 January 2014, at around 11:40 BJT.

As an illustration, Fig. 3 shows the changes in individual NO$_2$ DSCD$_{meas}$ and DSCD$_{offset}$ for a 30° elevation angle of each sequence as a function of time on 18 January 2014. As shown in Fig. 3, a second-order polynomial fitted from individual DSCD$_{offset}$ data points as shown in Fig. 3 tends to be stable and can be used to represent an average value of DSCD$_{offset}$.

2.3 LAPS-WRF-CMAQ model simulation

2.3.1 Model setup and data

To quantify the NO$_x$ emissions in Beijing more accurately, refined simulations of the wind field and NO$_2$-to-NO$_x$ concentration ratio were needed. In this study, we utilized the offline LAPS-WRF-CMAQ model system with a high spatiotemporal resolution and data assimilation technique to obtain the refined wind speed and wind direction and an accurate ratio of NO$_2$-and-NO$_x$ concentration during the car MAX-DOAS experiments. The aforementioned model system includes three components: the Local Analysis and Pre-

diction System (LAPS) model (Albers et al., 1996), the WRF model (Michalakes et al., 2004), and the CMAQ model (Dennis et al., 1996). Simulation of wind speed and direction is improved by the LAPS-WRF model, which assimilates observed data at the surface and high layers using the one-dimensional and three-dimensional variational assimilation methods (Albers et al., 1996). The CMAQ model is used to simulate the temporal–spatial distribution of NO$_2$ and NO concentration. The LAPS, developed by the NOAA Earth System Research Laboratory, is used in many numerical weather forecast centers around the world. It is a mesoscale meteorological data assimilation tool that employs a suite of observations to generate a realistic, spatially distributed, time-evolving, three-dimensional representation of atmospheric structures and processes (McGinley et al., 1991). The three-dimensional realistic meteorological analysis field can be used as the initial condition of the WRF model and improve the simulation of wind fields. WRF is a mesoscale numerical weather prediction system designed for both atmospheric research and operational forecasting needs.
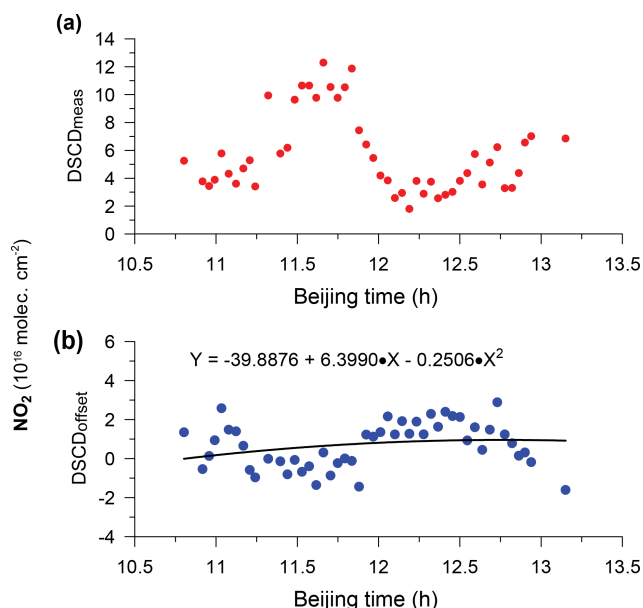
Figure 3. Time series of the NO$_2$ **(a)** DSCD$_{means}$ (red dots) and **(b)** DSCD$_{offset}$ (black dots) (units of 10^{16} molec. cm^{-2}) for the 30° elevation angle of each sequence on 18 January 2014. The black curve represents a second-order polynomial fit from individual DSCD$_{offset}$ data points.

CMAQ is an air-quality model developed by the U.S. Environmental Protection Agency's Atmospheric Science Modeling Division. It consists of a suite of computer programs for modeling air quality issues, including reactive gases such as NO$_2$, NO, SO$_2$, O$_3$, and others, particulate matter (PM), air toxins, acid deposition, and visibility degradation.

This study focused on Beijing at a horizontal resolution of 4 km × 4 km with 31 vertical layers of varying thickness (between the surface and 50 hPa) using a triple-nested simulation technique. The horizontal resolutions of the three sets of grids were 36, 12, and 4 km, respectively (Fig. S1a in the Supplement), and the output temporal interval was 1 h. The LAPS-WRF simulations were driven by FNL/NCEP analysis data every 6 h during the car MAX-DOAS experiments, with a spatial resolution of 1° × 1°. In addition, to improve the simulation of wind field and NO$_2$ and NO concentrations, many meteorological data of the same periods, such as wind speed, wind direction, air temperature, and relative humidity, observed at 2400 surface weather stations and 120 radiosonde stations were assimilated into the initial field of the WRF model using the one-dimensional and three-dimensional variational assimilation methods in the LAPS model. The CMAQ model uses the multi-resolution emission inventory in China for the year 2012 (MEIC 2012) with 0.25° × 0.25° resolution (Zhang et al., 2009; Li et al., 2017). Hourly gridded MEIC emission datasets at a horizontal resolution of 4 km × 4 km for the CMAQ model were generated by the Sparse Matrix Operator Kernel Emissions

(SMOKE) modeling system (UNC, 2014) using reasonable temporal and grid allocation factors (Cheng et al., 2017). Meteorological outputs from the WRF simulations were processed to create model-ready inputs for CMAQ using the Meteorology–Chemistry Interface Processor (MCIP) (Otte and Pleim, 2010). The chemical mechanism is CB05, and the boundary conditions of trace gases consist of idealized, Northern Hemispheric, mid-latitude profiles based on results from the NOAA Agronomy Lab Regional Oxidant Model. The model simulation was started 1 d before the first day of the experiment to avoid the spin-up problem and improve the simulation accuracy.

2.3.2 Validation of simulated surface wind and NO$_2$

Modeled wind speeds and directions were validated by observation data from four weather stations in Beijing. Figures S2, S3, and S4 show the scatter distribution between simulated wind speed and observation, the wind rose of modeled wind direction and measurements, and their time serials. We adopted the observed hourly wind speed and direction data from Nanjiao (NJ), Tongzhou (TZ), Mentougou (MTG), and Shunyi (SY) meteorological stations, which represent the southern, eastern, western, and northern areas of Beijing, respectively. It was shown that the temporal variations in simulated wind speed at the four stations were consistent with the observations from the perspective of time serial of wind speed, but the simulations were higher than the observations due to impacts of the complex topography and limited observation data assimilated to the LAPS-WRF model (Figs. S2 and S4a). To calculate the E_{NO_x} accurately, we corrected the simulated wind speed using the observation data from the four weather stations in order to reduce the systemic error. Specifically, we computed the relative error of the modeled wind speed based on measurements at four weather stations for each journey and then added the error bar to simulated wind speed at every sampling position during the same journey. The correlation coefficient between simulated and observed wind speeds at the four stations is 0.5, and the result passes the 99.9 % significance test. The root mean square error (RMSE) is small, with a value of 1.2 m s^{-1}. Except for the MTG station, simulated wind directions at the other three stations are in accordance with the observations, particularly for the primary wind direction (Figs. S3 and S4b). In general, simulated wind directions are also coincident with observations from the perspective of time serial of wind direction, and simulations are larger than measurements during some periods at some stations due to the effects of the complex topography and limited observation data assimilated to the model (Fig. S4b). The primary wind direction and its frequency at the MTG station are not consistent with the observations because these are affected by the complex topography near the Taihang and Yanshan mountains. In general, the corrected wind speed and wind direction data are reliable for estimation of the NO$_x$ emissions, and the uncertainty of

E_{NO_x} due to the variation of the wind field is discussed in Sect. 3.3.

Figure S4 presents the temporal variation in simulated and observed NO$_2$ concentration from 18 January to 13 October 2014. The hourly measurements of NO$_2$ concentrations (shown in Fig. S1b) were obtained from the National Environment Monitoring Station in China. In general, the temporal variation in the NO$_2$ simulation is consistent with the observation. The simulated values are close to the observations, except for 21–24 January, 19 September, and 9–10 October, when NO$_2$ simulations are higher than the observations (Fig. S5). The correlation coefficient between simulated and observed NO$_2$ concentrations is 0.7, and the result passes the 99.9 % significance test (Fig. S6). The RMSE and mean absolute error (MAE) are 16.1 and 19.2 µg m^{-3}, respectively. The observed NO$_2$ might include some NOz component, leading to a systematical bias (underestimation) of NO$_2$ by the model compared to observation (Ma et al., 2012). Thus, the simulated NO$_2$ concentrations and hence the ratio of NO$_2$ and NO$_x$ are reliable for estimating NO$_x$ emissions.

2.4 Selection of the journeys for estimating NO$_x$ emissions

To estimate the NO$_2$ fluxes (F_{NO_2}) and E_{NO_x} accurately, we firstly selected six journeys with the RMSEs of simulated wind speeds at the four weather stations smaller than 1.5 m s^{-1} from the primary selected 11 journeys. Then we assessed whether the meteorological and chemical conditions meet the criteria of Shaiganfar et al. (2017) for each of these six journeys or not. It should be pointed out that we cannot assess the problem of a large partitioning ratio due to the absence of the whole seasonal simulated or observed data in fall and winter. The assessment results of the other four problems are listed in Table 2. We excluded the journeys in which more than two problems occurred. It needs to be noted that lifetime correction coefficients c_τ on 12 and 13 October are slightly larger than 1.5, which is the criterion of a large lifetime correction (Shaiganfar et al., 2017), so we also adopted the data on 12 and 13 October to estimate the E_{NO_x}. Lastly, NO$_2$ VCD measurements outside of the 6th Ring Rd during five selected journeys were not used to quantify F_{NO_2} and E_{NO_x}.

3 Results and discussion

3.1 Tropospheric NO$_2$ VCD

Figure 4 presents the journey-to-journey temporal variation in the tropospheric NO$_2$ VCD on the 6th Ring Rd of Beijing in January, September, and October 2014. In general, the NO$_2$ VCD in January was higher than that in the other months. The highest values occurred on 19, 23, and 24 January. The mean NO$_2$ VCD ranged mostly from $4.5 \pm 1.8 \times 10^{16}$ to $9.0 \pm 1.2 \times 10^{16}$ molec. cm^{-2} in January, but val-
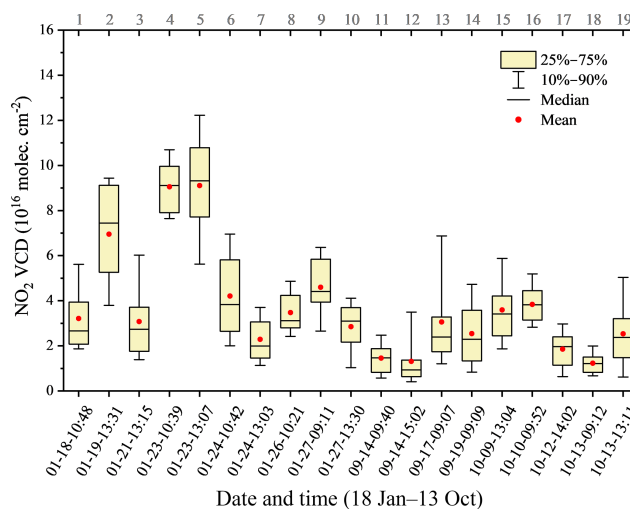

Figure 4. Time series of the tropospheric NO$_2$ vertical column density (VCD) for 19 circling journeys on the 6th Ring Rd of Beijing in January, September, and October 2014. Lower (upper) error bars and yellow boxes are the 10th (90th) and 25th (75th) percentiles of the data of each journey, respectively. Hyphens inside the boxes are the medians, and red circles are the mean values. The numbers of each journey are labeled on the top axis. See Table 1 for detailed information about each journey.

ues were all lower than 4.5×10^{16} molec. cm^{-2} in September and October. The NO$_2$ VCD values during the mornings of 23 January and 13 October were 9.1×10^{16} and 1.2×10^{16} molec. cm^{-2}, corresponding to the maximum and minimum values, respectively, during the 19 circling journeys. This result might be caused by higher emissions from coal-fired heating (Table S1 in the Supplement) and lower photolysis of NO$_2$ in winter. A similar pattern of seasonal variation in tropospheric NO$_2$ VCD was found previously by site MAX-DOAS measurements in Beijing (Ma et al., 2013a; Hendrick et al., 2014).

To investigate the differences in the spatial distribution of NO$_2$ VCD among the three months, we computed the monthly average NO$_2$ VCD for every sampling position along the 6th Ring Rd of Beijing in January, September, and October 2014 (Fig. 5). Firstly, we used the locations of all sampling positions in the morning of 23 September as the reference point for the calculation of NO$_2$ VCD monthly average, with the most sampling sites (98 points) for all observation periods. Then, we calculated the monthly average value at each reference point using the data of the nearest sampling position. The distance from the nearest sampling position to a reference point was less than 1.5 km. Figure 5 shows that the monthly average NO$_2$ VCD values at most sampling points on the 6th Ring Rd were obviously larger in January than in the other two months (by a factor of 2 in most cases). The spatial distribution characteristics of NO$_2$ VCD in September were similar to those in October. In addition, the NO$_2$ VCD values in the northern and southern parts of

Table 2. Overview of the problems for the six circling journeys.

Date	Time (BJT)	Large wind variability[a]	Large lifetime correction[a]	Gap/route close to the center[a]	Small difference between influx and outflux[a]	Multiple problems[b]
26 January 2014[c]	10:21–12:13	N	N	N	Y	N
27 January 2014[c]	13:30–15:28	Y	N	N	N	N
14 September 2014	09:40–12:52	Y	Y	Y	N	Y
14 September 2014[c]	15:02–17:17	N	Y	N	N	N
12 October 2014[c]	14:02–16:42	Y	Y	N	N	Y
13 October 2014[c]	09:12–11:59	Y	Y	N	N	Y

[a] Whether the condition meets the criteria of Shaiganfar et al. (2017) or not, Y and N denote Yes and No, respectively. [b] Multiple problems mean whether more than two conditions can meet the criteria or not. [c] The data of five circling journeys are ultimately used to estimate the NO$_x$ emission.
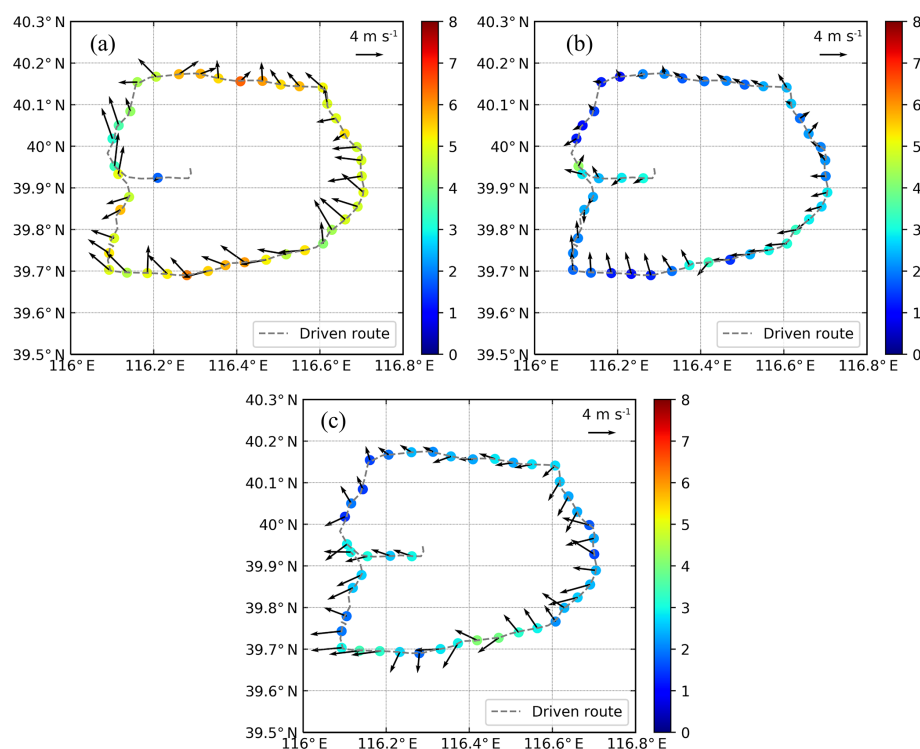
Figure 5. Distributions of monthly averaged NO$_2$ VCD (10^{16} molec. cm^{-2}) on the 6th Ring Rd of Beijing in **(a)** January, **(b)** September, and **(c)** October 2014.

the 6th Ring Rd were all larger than those in the other areas for all three months. The high NO$_2$ VCD in the southern region was related to strong local emissions to the south of Beijing and transport from central and southern Hebei and the city of Tianjin (Meng et al., 2018). As shown in Fig. 4, the maximum journey-averaged NO$_2$ VCD occurred on the morning of 23 January, and the minimum occurred on the morning of 13 October.

We investigated the spatial distribution differences in NO$_2$ VCD between these two circling journeys, as shown in Fig. 6. The NO$_2$ VCD values on the 6th Ring Rd in the morning of 23 January were all large, particularly in the northern and southwestern areas, with magnitudes of 10×10^{16} to 12×10^{16} molec. cm^{-2}. On 13 October, high NO$_2$ VCD

was located in the southern areas, and it might be related to the southern emission sources closer to the southern 6th Ring Rd, where its emission rates are obviously higher than the northern Ring Rd. The spatial distribution differences between these two journeys were related to the high emission during the heating season in January (see Sect. 3.2) and the impacts of the wind field. We used thin-grid ECWMF reanalysis data for 23 January and 13 October with a spatial resolution of $0.125° \times 0.125°$ to investigate the impact of the wind field on the spatial distribution of NO$_2$ VCD. Figure 7 shows the wind fields at 08:00 and 14:00 BJT on these two days, respectively. The NO$_2$ VCD was large, with weak southerly wind and convergence of southeasterly and northwesterly wind in Beijing and its surrounding area, but
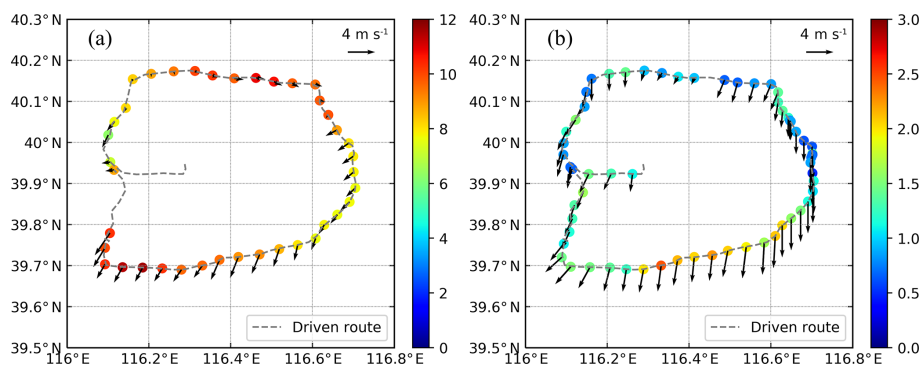
Figure 6. Distributions of the maximum and minimum NO$_2$ VCD (10^{16} molec. cm^{-2}) on the 6th Ring Rd of Beijing on the morning of **(a)** 23 January and **(b)** 13 October 2014.
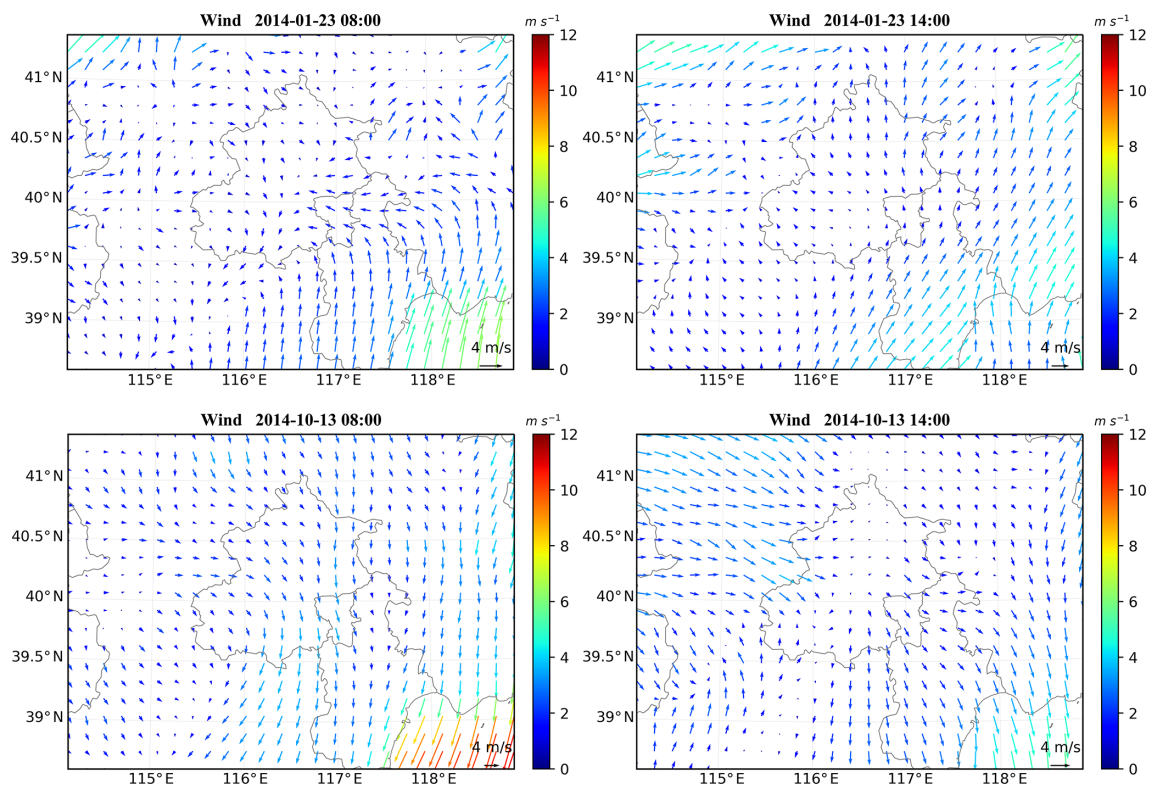

Figure 7. Wind fields in Beijing and the surrounding area from the ECWRF at 08:00 (left column) and 14:00 (right column) BJT on 23 January and 13 October 2014.

its values were far smaller, with strong northerly wind. Weak southerly wind and a breeze or calm wind resulted in the transport of NO$_2$ from the southern area in Hebei Province and its accumulation on 23 January. Strong northerly wind suppressed the transport of NO$_2$ from the southern area on 13 October. These results indicate that the wind field has large impacts on the spatial distribution of NO$_2$ VCD in Beijing.

Figure 8 presents the spatial distributions of wind and NO$_2$ VCD averaged for the two different wind fields. The mean NO$_2$ VCD at most sampling positions along the 6th Ring Rd was obviously higher under the southerly wind field than the northerly wind. High NO$_2$ emission sources were located within the 5th Ring Rd of Beijing in the three months (Fig. 10), and the background concentrations of NO$_2$ VCD in the northern and southern areas were remarkably different due to the impacts of emission sources on the south of Beijing. Hence, southerly wind can transfer air pollutants from the southern area to Beijing and lead to high NO$_2$ flux, whereas impacts of northerly wind on NO$_2$ flux are smaller because the background concentrations of NO$_2$ VCD in the north of Beijing were lower. Convergence of the wind field in
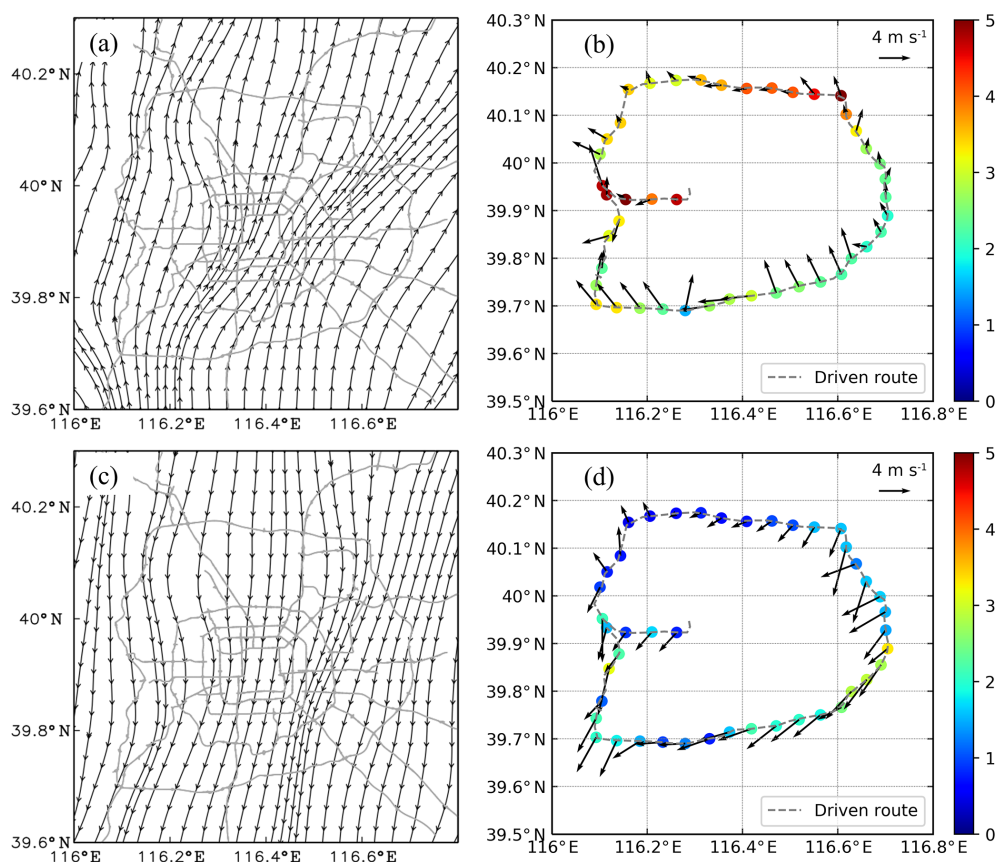
Figure 8. Average wind stream and NO$_2$ VCD (10^{16} molec. cm^{-2}) distributions under the two different types of wind field over Beijing: **(a)** southerly wind, **(b)** NO$_2$ VCD under southerly wind, **(c)** northerly wind, and **(d)** NO$_2$ VCD under northerly wind.

the southern parts of the 6th Ring Rd is favorable to the accumulation of NO$_2$ from the surrounding area to the southern parts of the ring road.

3.2 Quantification of NO$_x$ emissions

Figure 9 shows the journey-to-journey variation of the estimated F_{NO_2} and E_{NO_x} over Beijing for five circling journeys in January, September, and October 2014. The F_{NO_2} fell in between 1.9×10^{25} and 15.7×10^{25} molec. s^{-1}. The ranges of E_{NO_x} during the heating (January) and non-heating (September and October) periods were 22.6×10^{25} to 31.3×10^{25} and 9.6×10^{25} to 12.0×10^{25} molec. s^{-1}, respectively. The average E_{NO_x} values in the heating and non-heating periods were $26.9 \pm 6.1 \times 10^{25}$ and $11.0 \pm 1.2 \times 10^{25}$ molec. s^{-1}, respectively. In general, the journey-to-journey variation patterns of F_{NO_2} and E_{NO_x} are consistent with that of the mean NO$_2$ VCD. In other words, the estimate of E_{NO_x} is determined mainly by the NO$_2$ VCD. Seasonal variation characteristics of the estimated E_{NO_x} were obvious. Specifically, the total E_{NO_x} was higher in January than in the other two months. The average E_{NO_x} in the heating period was about 2.5 times as much as those in the non-heating period. The coal-fired heating in Beijing included central heating in the

urban area and scattered coal combustion in the suburbs or rural area for the year 2014. We calculated the average NO$_x$ emission rates of four sectors, including industry, power, residential, and transportation, from the MEIC within the 6th Ring Rd of Beijing in January, September, and October 2012 and the ratio of each specific NO$_x$ emission rate in January to the corresponding average value in September and October (Table S1). The E_{NO_x} from the power and residential sections was remarkably higher in January than in the other two months, and especially E_{NO_x} from the residential sector was in January 5.4 times as much as those in the other two months. In general, central heating in the urban area is from power plant and residential use of the scattered coal combustion in the suburbs or rural area.

In addition to the seasonal differences, the journey-to-journey variation in estimated E_{NO_x} is large even within the same month, mainly due to uncertainties in the calculations of wind speed, the ratio of NO$_2$ and NO$_x$ concentration, and the decay rate of NO$_x$ from the emission sources to the measured positions under different meteorological conditions. In addition to the NO$_2$ VCD, wind speed, and wind direction at the sampling positions, the estimated NO$_x$ emission rate is obviously affected by the Leighton ratio of NO and NO$_2$ con-
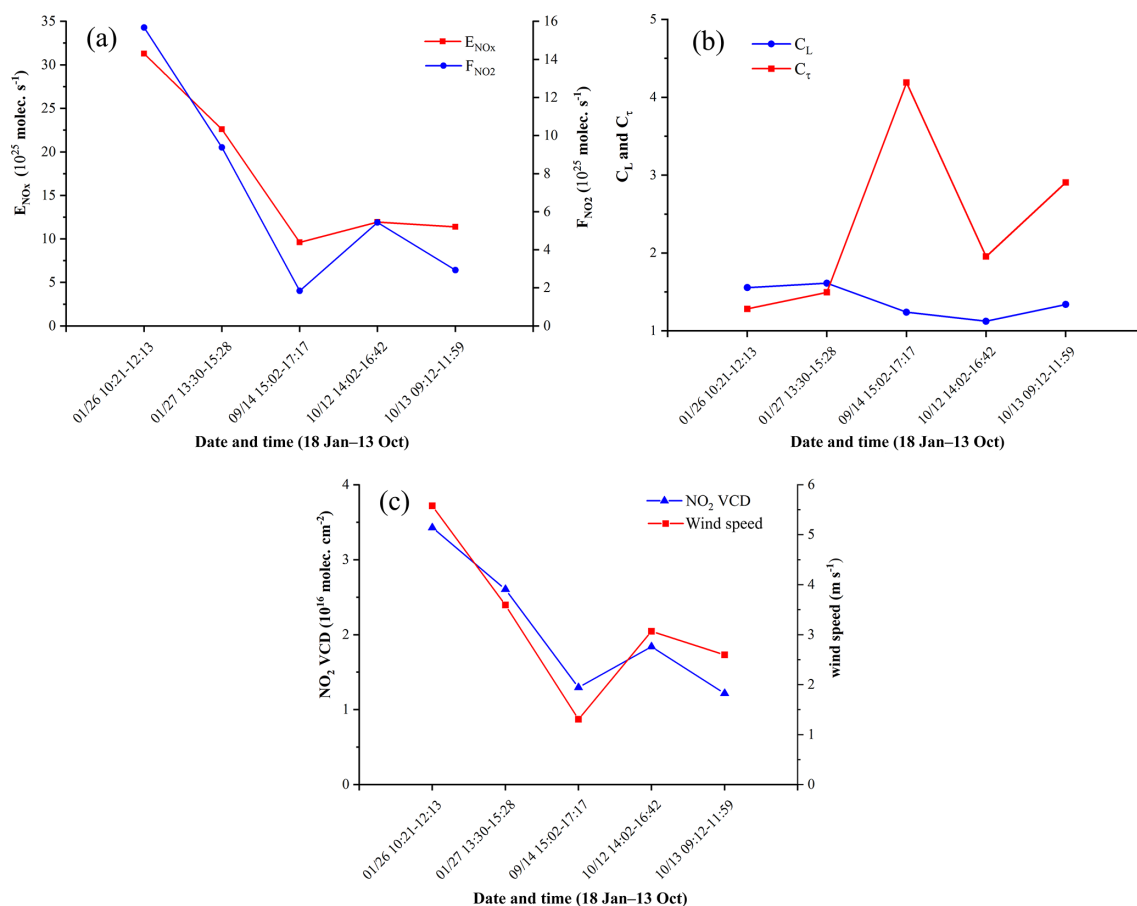
Figure 9. Journey-to-journey variations in **(a)** F_{NO_2} and E_{NO_x}, **(b)** c_τ and c_L, and **(c)** NO$_2$ VCD and mean wind speed for five circling journeys on the 6th Ring Rd of Beijing in January, September, and October 2014.

centration and the lifetime of NO$_x$ (Valin et al., 2013). Thus, the estimated NO$_x$ emission rate could be very large even if the NO$_2$ VCD was small, such as in the case of 14 September. It should be noted that the low mean wind speed on 14 September leads to high c_τ, so the E_{NO_x} for this journey is not too small, although the F_{NO_2} was very low. In addition, if both c_τ and c_L are large, high E_{NO_x} can be derived.

3.3 Comparisons with the MEIC inventory

We compared the estimated NO$_x$ emission with the MEIC 2012 (Zhang et al., 2009, 2012). The horizontal resolution of MEIC 2012 is $0.25° \times 0.25°$, and five sectors, i.e., agriculture, industry, power, residential, and transportation, are included.

Figure 10 presents the spatial distributions of NO$_x$ emission rates from MEIC over Beijing in January, September, and October 2012. A high NO$_x$ emission zone was located within the 5th Ring Rd of Beijing, and low emissions occurred in its surroundings. The NO$_x$ emissions in January were obviously larger than those in the other two months.

Figure 11 shows the estimated NO$_x$ emission rates from car MAX-DOAS measurements for each selected journey (see Sect. 2.4) in January, September, and October 2014 and the corresponding monthly averaged NO$_x$ emission rates from the MEIC 2012 for the same region within the 6th Ring Rd of Beijing (hereafter expressed as MEIC_Month). The MEIC_Month is obviously lower than the estimated E_{NO_x} in January. While the two emission estimates are very close in September, the MEIC_Month is slightly smaller than the E_{NO_x} in October. The differences between the estimated E_{NO_x} and the MEIC_Month during some journeys were remarkably large, which may be caused by (1) the interannual variations in the emission inventory, (2) the different timescales of the two emission estimates, and (3) the uncertainty of the estimated E_{NO_x} and MEIC 2012. Firstly, the E_{NO_x} in this study is estimated for the year 2014, whereas the MEIC_Month was established for the year 2012. Secondly, our results represent only the conditions during a few measurements in the daytime, whereas the MIEC 2012 denoted monthly average conditions. Thirdly, the uncertainty of the MEIC 2012 is large, particularly in fall and winter (Li et al., 2017; Meng et al., 2018). There are also large uncertainties in
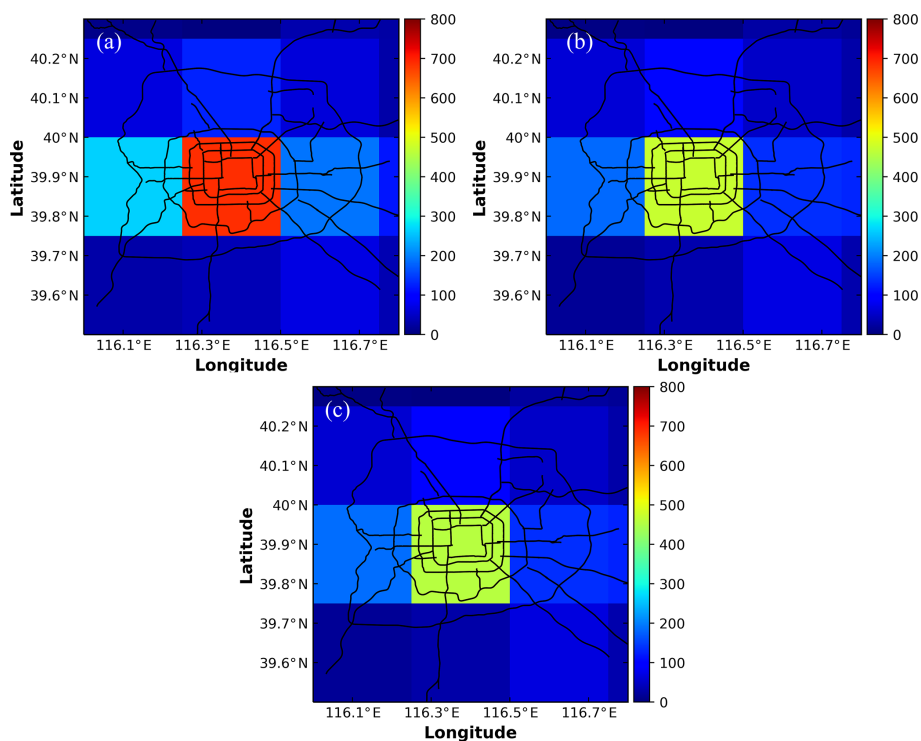
Figure 10. Spatial distributions of monthly averaged NO$_x$ emission rate (mol km^{-2} h^{-1}) over Beijing based on the MEIC inventory in **(a)** January, **(b)** September, and **(c)** October in 2012.
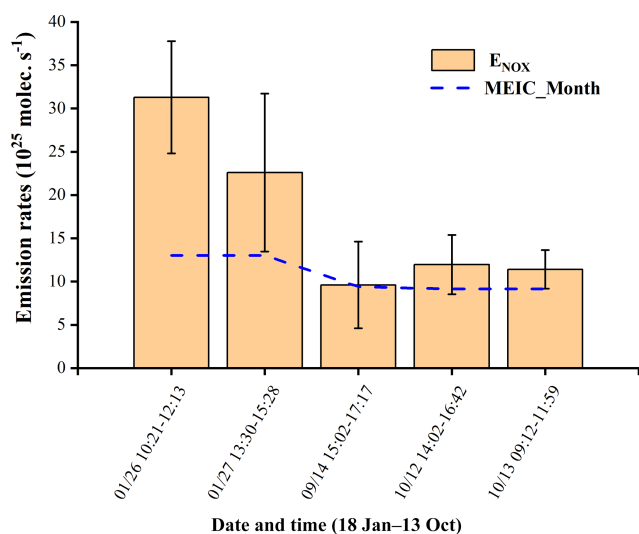

Figure 11. Journey-to-journey variations in estimated E_{NO_x} and corresponding monthly emission rate from the MEIC inventory (MEIC_Month) within the 6th Ring Rd of Beijing in January, September, and October 2014. Error bars represent the uncertainties in estimated E_{NO_x}.

the estimated E_{NO_x} caused by, e.g., the inconsistency of the wind field during a circling journey and the transfer of NO$_2$ from other source areas than urban Beijing. The CIM assumes that the wind field is constant during the measurement period and that the wind speed is also sufficiently high. However, the wind field during some journeys (27 January and 12 and 13 October) might have changed systematically. Ibrahim et al. (2010) also pointed out that systematic changes during the measurements period can have large impacts on the emission estimate, particularly if measurements with high trace gas VCD are accompanied by strong deviations of the actual wind speed (or direction) from the assumed average values. For example, on the afternoon of 27 January, high NO$_2$ VCD was measured, and the wind field changed during the measurement journey. In such cases, the systematic changes in wind speed and direction can lead to additional uncertainties in E_{NO_x}. Moreover, because the southerly wind can bring NO$_x$ emitted in the southern–central regions of Hebei Province to Beijing, the E_{NO_x} from car MAX-DOAS measurements will be overestimated under southerly wind conditions, e.g., on 26 January.

3.4 Uncertainty analysis of estimated emissions

We calculated the uncertainty of E_{NO_x} according to the error transfer formula of relative deviation based on the errors of measured NO$_2$ VCD and simulated wind speed and direc-

Table 3. Error contributions (%) of multiple factors to the uncertainties in estimated E_{NO_x} during five circling journeys.

Factors	26 January, AM	27 January, PM	14 September, PM	12 October, PM	13 October, AM
VCD$_{geo}$	10	10	10	10	10
Wind speed	27.02	26.83	7.97	33.10	3.68
Wind direction	10.97	16.50	20.54	33.78	38.37
NO$_x$/NO$_2$ ratio	12.21	13.46	7.82	29.33	29.48
Lifetime	3.63	7.67	48.60	15.22	19.02

tion, c_L and c_τ. The standard deviation (SD) of wind speed over a period of time can provide a bound for the related uncertainties of the emission estimate (Ibrahim et al., 2010). Therefore, we first computed the uncertainty of F_{NO_2} based on the SD of simulated wind speed after correction and the measurement error of NO$_2$ VCD (about $\pm 10\%$, Ma et al., 2013a) for each journey. Then, we calculated the SD of c_τ according to the first derivative of Eq. (4) and the SD of c_L using a different NO$_x$ lifetime and the ratios of NO$_x$ and NO$_2$ at sampling positions on the 6th Ring Rd of Beijing for each journey. Figure 11 shows the uncertainties of E_{NO_x} for five journeys, and the uncertainty range of E_{NO_x} is 2.2×10^{25} to 9.1×10^{25} molec. s^{-1} (20 %–52 %).

We also give the spatial variation in the NO$_x$/NO$_2$ ratio and NO$_x$ lifetime at the entire route for the emission calculation during five journeys (Figs. S7 and S8) and estimate the error contribution of five factors, including NO$_2$ VCD, wind speed, wind direction, the NO$_x$/NO$_2$ ratio, and the NO$_x$ lifetime to the total uncertainty of E_{NO_x} (Table 3). In general, there are obvious seasonal and regional differences in the NO$_x$/NO$_2$ ratio and NO$_x$ lifetime, and it is necessary to use specific ratios and lifetime values to estimate the E_{NO_x} for each journey. Specifically, the NO$_x$/NO$_2$ ratio and NO$_x$ lifetime are larger in January than September and October, and they are larger at the southern part of the 6th Ring Rd than in other parts for most journeys. Among error contributions of the five factors, the impacts of wind speed and direction are the largest for most journeys except for 14 September. For 26 and 27 January, error contributions of wind speed to the uncertainty of E_{NO_x} are larger than the other four factors. For 14 September, uncertainty of E_{NO_x} is mainly caused by the errors of NO$_x$ lifetime and wind direction. For 12 and 13 October, error contributions of the NO$_x$/NO$_2$ ratio are also remarkable. Thus, it is important to obtain the accurate wind vector profiles, NO$_x$, NO$_2$, and OH concentration data besides measured NO$_2$ VCD to reduce the uncertainty of E_{NO_x} estimation using the CIM.

We also calculate the Leighton ratios, L_r, to assess impacts of VOCs on the NO$_x$ lifetime. The L_r during five journeys is 0.85, 0.80, 1.04, 1.19, and 1.33 on 26 and 27 January, 14 September, and 12 and 13 October, respectively. Results show that VOCs can affect the NO$_x$ lifetime, which leads to extra errors of E_{NO_x} for the three journeys in September and October, while the uncertainty in VOCs causes insignificant deviations in the NO$_x$ lifetime and E_{NO_x} estimation in January.

4 Conclusions

We carried out 19 city-circle-around car MAX-DOAS experiments on the 6th Ring Rd of Beijing in January, September, and October 2014. The VCD of NO$_2$ was retrieved, and the temporal and spatial distributions were investigated. Then the NO$_x$ emission rates in urban Beijing were estimated using the measured NO$_2$ VCD together with the refined wind fields, NO$_2$-to-NO$_x$ ratios, and NO$_2$ lifetimes simulated by the LAPS-WRF-CMAQ model system, and the results were compared to the emission rates from the MEIC 2012.

The NO$_2$ VCD values averaged for each experimental journey in January were all larger than those in the other 2 months, mainly due to higher emissions in winter. The measured NO$_2$ VCD was typically larger in the southern parts of the 6th Ring Road than in the northern parts because weak southerly wind resulted in the transport and accumulation of NO$_2$ from southern areas in Hebei Province and strong northerly wind suppressed the transport of NO$_2$ from the southern area. Such inhomogeneous distributions of tropospheric NO$_2$ VCD bring a challenge for the validation of satellite products for Beijing as well as other megacities.

The journey-to-journey variations in estimated E_{NO_x} were large, even within the same month, mainly due to uncertainties in the calculation of wind speed, the ratio of NO$_2$ and NO$_x$ concentration, and the decay rate of NO$_x$ from the emission sources to the measured positions under different meteorological conditions. The average E_{NO_x} values in the heating and non-heating periods are estimated to be $26.9 \pm 6.1 \times 10^{25}$ and $11.0 \pm 1.2 \times 10^{25}$ molec. s^{-1}, respectively, with an uncertainty range of 20 %–52 %. The monthly emission rates in the area within the 6th Ring Rd of Beijing from MEIC 2012 are lower than the estimated E_{NO_x}, particularly in January. The differences between the E_{NO_x} and the monthly emission rates from MEIC 2012 can be attributed to the interannual differences in the emission inventory, the different timescales, and uncertainties of two kinds of inventories.

Our results show that car MAX-DOAS measurements can be used effectively for dynamic monitoring and updating of the NO$_x$ emissions in megacities such as Beijing. To accurately estimate the E_{NO_x} by car MAX-DOAS in Beijing and

other similar megacities, appropriate meteorological conditions, such as small fluctuations of the wind field, relatively larger wind speed, and suitable wind direction, need to be selected to avoid the impact of extra transfers of large emission sources from surrounding areas. In addition to the NO$_2$ VCD, simultaneous observations of wind speed, wind direction, and surface NO and NO$_2$ concentrations are recommended to reduce the uncertainties of E_{NO_x}.

Author contributions. JM and XC designed the research. JM, JJ, JG, MQ, QX, and PY contributed to the measurements, and JM performed the spectral analysis and retrieval. XC and JP designed the model experiment and performed the model simulations. XC, YL, JP, and XM contributed to the data processing and analyses. XC and JM analyzed the results and wrote the paper with inputs from all the authors.

References

Albers, S. C., McGinley, J. A., Birkenheuer, D., and Smart, J. R.: The local analysis and prediction system (LAPS): Analyses of clouds, precipitation, and temperature, Weather Forecast., 11, 273–287, 1996.

Brinksma, E. J., Pinardi, G., Volten, H., Braak, R., Richter, A., Schoenhardt, A., van Roozendael, M., Fayt, C., Hermans, C., Dirksen, R. J., Vlemmix, T., Berkhout, A. J. C., Swart, D. P. J., Oetjen, H., Wittrock, F., Wagner, T., Ibrahim, O. W., de Leeuw, G., Moerman, M., Curier, R. L., Celarier, E. A., Cede, A., Knap, W. H., Veefkind, J. P., Eskes, H. J., Allaart, M., Rothe, R., Piters, A. J. M., and Levelt, P. F.: The 2005 and 2006 DANDELIONS NO$_2$ and aerosol intercomparison campaigns, J. Geophys. Res.-Atmos., 113, D16S46, https://doi.org/10.1029/2007JD008808, 2008.

Burrows, J. P., Richter, A., Dehn, A., Deters, B., Himmelmann, S., Voigt, S., and Orphal, J.: Atmospheric remote sensing reference data from GOME-2. temperature-dependent absorption cross-sections of O$_3$ in the 231–794 nm range, J. Quant. Spectrosc. Ra., 61, 509–517, 1999.

Cao, C., Jiang, W., Wang, B., Fang, J., Lang, J., Tian, G., Jiang, J., and Zhu, T. F.: Inhalable microorganisms in Beijing's PM$_{2.5}$ and PM$_{10}$ pollutants during a severe smog event, Environ. Sci. Technol., 48, 1499–1507, https://doi.org/10.1021/es4048472, 2014.

Cheng, X., Sun, Z., Li, D., Xu, X., Jia, M., and Cheng, S.: Short-term aerosol radiative effects and their regional difference during heavy haze episodes in January 2013 in China, Atmos. Environ., 165, 248-263, https://doi.org/10.1016/j.atmosenv.2017.06.040, 2017.

China National Environmental Monitoring Centre: Real-time National Air Quality data, available at: http://www.cnemc.cn/en and http://data.cma.cn/, last access: September 2020.

Davis, Z. Y. W., Baray, S., McLinden, C. A., Khanbabakhani, A., Fujs, W., Csukat, C., Debosz, J., and McLaren, R.: Estimation of NO$_x$ and SO$_2$ emissions from Sarnia, Ontario, using a mobile MAX-DOAS (Multi-AXis Differential Optical Absorption Spectroscopy) and a NO$_x$ analyzer, Atmos. Chem. Phys., 19, 13871–13889, https://doi.org/10.5194/acp-19-13871-2019, 2019.

Dennis, R., Byun, D., and Novak, J.: The next generation of integrated air quality modeling: EPA's Models-3, Atmos. Environ., 30, 1925–1938, 1996.

Dickerson, R. R., Stedman, D. H., and Delany, A. C.: Direct measurements of ozone and nitrogen dioxide photolysis rates in the troposphere, J. Geophys. Res., 87, 4933–4946, https://doi.org/10.1029/JC087iC07p04933, 1982.

European Centre for Medium-Range Weather Forecasts: ERA Interim data, available at: https://apps.ecmwf.int/datasets/data/interim-full-daily/levtype=sfc, last access: August 2019.

Fayt, C. and Van Roozendael, M.: WinDOAS 2.1 software user manual, IASB/BIRA Uccle, Belgium, 2011.

Greenblatt, G. D., Orlando, J. J., Burkholder, J. B., and Ravishankara, A. R.: Absorption measurements of oxygen between 330 and 1140 nm, J. Geophys. Res., 95, 18577–18582, https://doi.org/10.1029/JD095iD11p18577, 1990.

Hönninger, G. and Platt, U.: Observations of BrO and its vertical distribution during surface ozone depletion at Alert, Atmos. Environ., 36, 2481–2489, https://doi.org/10.1016/S1352-2310(02)00104-8, 2002.

Hönninger, G., von Friedeburg, C., and Platt, U.: Multi axis differential optical absorption spectroscopy (MAX-DOAS), Atmos. Chem. Phys., 4, 231–254, https://doi.org/10.5194/acp-4-231-2004, 2004.

Hao, J., Tian, H., and Lu, Y.: Emission inventories of NO$_x$ from commercial energy consumption in China, 1995–1998, Environ. Sci. Technol., 36, 552–560, 2002.

He, H., Wang, X. M., Wang, Y. S., Wang, Z. F., Liu, J. G., and Chen, Y. F.: Formation Mechanism and Control Strategies of Haze in China, Bull. Chin. Acad. Sci., 28, 344–352, 2013.

Hendrick, F., Müller, J.-F., Clémer, K., Wang, P., De Mazière, M., Fayt, C., Gielen, C., Hermans, C., Ma, J. Z., Pinardi, G., Stavrakou, T., Vlemmix, T., and Van Roozendael, M.: Four years of ground-based MAX-DOAS observations of HONO and NO$_2$ in the Beijing area, Atmos. Chem. Phys., 14, 765–781, https://doi.org/10.5194/acp-14-765-2014, 2014.

Huang, R. J., Zhang, Y., Bozzetti, C., Ho, K. F., Cao, J. J., Han, Y., Daellenbach, K. R., Slowik, J. G., Platt, S. M., Canonaco, F., Zotter, P., Wolf, R., Pieber, S. M., Bruns, E. A., Crippa, M., Ciarelli, G., Piazzalunga, A., Schwikowski, M., Abbaszade, G., Schnelle-Kreis, J., Zimmermann, R., An, Z., Szidat, S., Baltensperger, U., El Haddad, I., and Prevot, A. S.: High secondary aerosol contribution to particulate pollution during haze events in China, Nature, 514, 218–222, https://doi.org/10.1038/nature13774, 2014.

Ibrahim, O., Shaiganfar, R., Sinreich, R., Stein, T., Platt, U., and Wagner, T.: Car MAX-DOAS measurements around entire cities: quantification of NO$_x$ emissions from the cities of Mannheim and Ludwigshafen (Germany), Atmos. Meas. Tech., 3, 709–721, https://doi.org/10.5194/amt-3-709-2010, 2010.

Irie, H., Kanaya, Y., Akimoto, H., Tanimoto, H., Wang, Z., Gleason, J. F., and Bucsela, E. J.: Validation of OMI tropospheric NO$_2$ column data using MAX-DOAS measurements deep inside the North China Plain in June 2006: Mount Tai Experiment 2006, Atmos. Chem. Phys., 8, 6577–6586, https://doi.org/10.5194/acp-8-6577-2008, 2008.

Jaeglé, L., Steinberger, L., Martin, R. V., and Chance, K.: Global partitioning of NO$_x$ sources using satellite observations: relative roles of fossil fuel combustion, biomass burning and soil emissions, Roy. Soc. Chem., 130, 407–423, 2005.

Jin, J., Ma, J., Lin, W., Zhao, H., Shaiganfar, R., Beirle, S., and Wagner, T.: MAX-DOAS measurements and satellite validation of tropospheric NO$_2$ and SO$_2$ vertical column densities at a rural site of North China, Atmos. Environ., 133, 12–25, https://doi.org/10.1016/j.atmosenv.2016.03.031, 2016.

Johansson, M., Galle, B., Yu, T., Tang, L., Chen, D., Li, H., Li, J. X., and Zhang, Y.: Quantification of total emission of air pollutants from Beijing using mobile mini-DOAS, Atmos. Environ., 42, 6926–6933, https://doi.org/10.1016/j.atmosenv.2008.05.025, 2008.

Johansson, M., Rivera, C., de Foy, B., Lei, W., Song, J., Zhang, Y., Galle, B., and Molina, L.: Mobile mini-DOAS measurement of the outflow of NO$_2$ and HCHO from Mexico City, Atmos. Chem. Phys., 9, 5647–5653, https://doi.org/10.5194/acp-9-5647-2009, 2009.

Konovalov, I. B., Beekmann, M., Richter, A., and Burrows, J. P.: Inverse modelling of the spatial distribution of NO$_x$ emissions on a continental scale using satellite data, Atmos. Chem. Phys., 6, 1747–1770, https://doi.org/10.5194/acp-6-1747-2006, 2006.

Kraus, S.: DOASIS, DOAS for Windows software [CD-ROM], in: Proceedings of the 1st International DOAS-Workshop, 13–14 September 2001, Heidelberg, Germany, 2001.

Li, M., Liu, H., Geng, G., Hong, C., Liu, F., Song, Y., Tong, D., Zheng, B., Cui, H., Man, H., Zhang, Q., and He, K.: Anthropogenic emission inventories in China: a review, Natl. Sci. Rev., 4, 834–866, https://doi.org/10.1093/nsr/nwx150, 2017.

Li, X., Brauers, T., Hofzumahaus, A., Lu, K., Li, Y. P., Shao, M., Wagner, T., and Wahner, A.: MAX-DOAS measurements of NO$_2$, HCHO and CHOCHO at a rural site in Southern China, Atmos. Chem. Phys., 13, 2133–2151, https://doi.org/10.5194/acp-13-2133-2013, 2013.

Liao, L., Lou, S. J., Fu, Y., Chang, W. J., and Liao, H.: Radiative forcing of aerosols and its impact on surface air temperature on the synoptic scale in eastern China, Chin. J. Atmos. Sci., 39, 68–82, 2015.

Lin, J.-T., Liu, Z., Zhang, Q., Liu, H., Mao, J., and Zhuang, G.: Modeling uncertainties for tropospheric nitrogen dioxide columns affecting satellite-based inverse modeling of nitrogen oxides emissions, Atmos. Chem. Phys., 12, 12255–12275, https://doi.org/10.5194/acp-12-12255-2012, 2012.

Ma, J. and van Aardenne, J. A.: Impact of different emission inventories on simulated tropospheric ozone over China: a regional chemical transport model evaluation, Atmos. Chem. Phys., 4, 877–887, https://doi.org/10.5194/acp-4-877-2004, 2004.

Ma, J. Z., Wang, W., Chen, Y., Liu, H. J., Yan, P., Ding, G. A., Wang, M. L., Sun, J., and Lelieveld, J.: The IPAC-NC field campaign: a pollution and oxidization pool in the lower atmosphere over Huabei, China, Atmos. Chem. Phys., 12, 3883–3908, https://doi.org/10.5194/acp-12-3883-2012, 2012.

Ma, J. Z., Beirle, S., Jin, J. L., Shaiganfar, R., Yan, P., and Wagner, T.: Tropospheric NO$_2$ vertical column densities over Beijing: results of the first three years of ground-based MAX-DOAS measurements (2008–2011) and satellite validation, Atmos. Chem. Phys., 13, 1547–1567, https://doi.org/10.5194/acp-13-1547-2013, 2013a.

Ma, J. Z., Wang, W., Liu, H., Chen, Y., Xu, X., and Lelieveld, J.: Pollution plumes observed by aircraft over North China during the IPAC-NC field campaign, Chinese Sci. Bull., 58, 4329–4336, https://doi.org/10.1007/s11434-013-5978-9, 2013b.

Martin, R. V.: An improved retrieval of tropospheric nitrogen dioxide from GOME, J. Geophys. Res., 107, ACH 9-1–ACH 9-21, https://doi.org/10.1029/2001jd001027, 2002.

McGinley, J. A., Albers, S., and Stamus, P.: Validation of a composite convective index as defined by a real-time local analysis system, Weather Forecast., 6, 337–356, 1991.

Meng, K., Xu, X., Cheng, X., Xu, X., Qu, X., Zhu, W., Ma, C., Yang, Y., and Zhao, Y.: Spatio-temporal variations in SO$_2$ and NO$_2$ emissions caused by heating over the Beijing-Tianjin-Hebei Region constrained by an adaptive nudging method with OMI data, Sci. Total Environ., 642, 543–552, https://doi.org/10.1016/j.scitotenv.2018.06.021, 2018.

Michalakes, J., Dudhia, J., Gill, D., Henderson, T., Klemp, J., Skamarock, W., and Wang, W.: The weather research and forecast model: software architecture and performance, the 11th ECMWFWorkshop on the Use of High Performance Computing In Meteorology, World Scientific Publishing Co Pte Ltd, Singapore, George Mozdzynski, 2004.

National Center for Atmospheric Research: NCEP FNL Operational Model Global Tropospheric Analyses data, available at: https://doi.org/10.5065/D6M043C6, last access: September 2020.

Otte, T. L. and Pleim, J. E.: The Meteorology-Chemistry Interface Processor (MCIP) for the CMAQ modeling system: updates through MCIPv3.4.1, Geosci. Model Dev., 3, 243–256, https://doi.org/10.5194/gmd-3-243-2010, 2010.

Platt, U.: Differential optical absorption spectroscopy (DOAS), in: Air Monitoring by Spectroscopic Techniques, edited by: Sigrist, M. W., Chemical Analysis Series, Vol. 127, John Wiley, New York, 27–84, 1994.

Platt, U. and Stutz, J.: Differential Optical Absorption Spectroscopy Principles and Applications, Physics of Earth and Space Environments, Springer, Heidelberg, 2008.

Shaiganfar, R., Beirle, S., Sharma, M., Chauhan, A., Singh, R. P., and Wagner, T.: Estimation of NO$_x$ emissions from Delhi using Car MAX-DOAS observations and comparison with OMI satellite data, Atmos. Chem. Phys., 11, 10871–10887, https://doi.org/10.5194/acp-11-10871-2011, 2011.

Shaiganfar, R., Beirle, S., Denier van der Gon, H., Jonkers, S., Kuenen, J., Petetin, H., Zhang, Q., Beekmann, M., and Wagner, T.: Estimation of the Paris NO$_x$ emissions from mobile MAX-DOAS observations and CHIMERE model simulations during the MEGAPOLI campaign using the closed integral method, Atmos. Chem. Phys., 17, 7853–7890, https://doi.org/10.5194/acp-17-7853-2017, 2017.

Streets, D. G., Canty, T., Carmichael, G. R., de Foy, B., Dickerson, R. R., Duncan, B. N., Edwards, D. P., Haynes, J. A., Henze, D. K., Houyoux, M. R., Jacob, D. J., Krotkov, N. A., Lamsal, L. N., Liu, Y., Lu, Z., Martin, R. V., Pfister, G. G., Pinder, R. W., Salawitch, R. J., and Wecht, K. J.: Emissions estimation from satellite retrievals: A review of current capability, Atmos. Environ., 77, 1011–1042, https://doi.org/10.1016/j.atmosenv.2013.05.051, 2013.

Tan, T., Hu, M., Li, M., Guo, Q., Wu, Y., Fang, X., Gu, F., Wang, Y., and Wu, Z.: New insight into PM$_{2.5}$ pollution patterns in Beijing based on one-year measurement of chemical compositions, Sci. Total Environ., 621, 734–743, https://doi.org/10.1016/j.scitotenv.2017.11.208, 2018.

UNC: SMOKE v3.6 user's manual, The institute for the Environment, Chapel Hill, 2014.

Valin, L. C., Russell, A. R., and Cohen, R. C.: Variations of OH radical in an urban plume inferred from NO$_2$ column measurements, Geophys. Res. Lett., 40, 1856–1860, https://doi.org/10.1002/grl.50267, 2013.

Vandaele, A. C., Hermans, C., Simon, P. C., Carleer, M., Colin, R., Fally, S., Mérienne, M. F., Jenouvrier, A., and Coquart, B.: Measurements of the NO$_2$ absorption cross-section from $42\,000\,cm^{-1}$ to $10\,000\,cm^{-1}$ (238–1000 nm) at 220 K and 294 K, J. Quant. Spectrosc. Ra., 59, 171–184, 1998.

Vlemmix, T., Piters, A. J. M., Stammes, P., Wang, P., and Levelt, P. F.: Retrieval of tropospheric NO$_2$ using the MAX-DOAS method combined with relative intensity measurements for aerosol correction, Atmos. Meas. Tech., 3, 1287–1305, https://doi.org/10.5194/amt-3-1287-2010, 2010.

Wagner, T., Dix, B., Friedeburg, C. v., Frieß, U., Sanghavi, S., Sinreich, R., and Platt, U.: MAX-DOAS O$_4$ measurements: A new technique to derive information on atmospheric aerosols – Principles and information content, J. Geophys. Res., 109, D22205, https://doi.org/10.1029/2004jd004904, 2004.

Wagner, T., Ibrahim, O., Shaiganfar, R., and Platt, U.: Mobile MAX-DOAS observations of tropospheric trace gases, Atmos. Meas. Tech., 3, 129–140, https://doi.org/10.5194/amt-3-129-2010, 2010a.

Wagner, T., Ibrahim, O., Shaiganfar, R., and Platt, U.: Mobile MAX-DOAS observations of tropospheric trace gases, Atmos. Meas. Tech., 3, 129–140, https://doi.org/10.5194/amt-3-129-2010, 2010b.

Wagner, T., Beirle, S., Brauers, T., Deutschmann, T., Frieß, U., Hak, C., Halla, J. D., Heue, K. P., Junkermann, W., Li, X., Platt, U., and Pundt-Gruber, I.: Inversion of tropospheric profiles of aerosol extinction and HCHO and NO$_2$ mixing ratios from MAX-DOAS observations in Milano during the summer of 2003 and comparison with independent data sets, Atmos. Meas. Tech., 4, 2685–2715, https://doi.org/10.5194/amt-4-2685-2011, 2011.

Wang, S., Zhou, B., Wang, Z., Yang, S., Hao, N., Valks, P., Trautmann, T., and Chen, L.: Remote sensing of NO$_2$ emission from the central urban area of Shanghai (China) using the mobile DOAS technique, J. Geophys. Res.-Atmos., 117, D13305, https://doi.org/10.1029/2011jd016983, 2012.

Wang, Y., McElroy, M. B., Martin, R. V., Streets, D. G., Zhang, Q., and Fu, T.-M.: Seasonal variability of NO$_x$ emissions over east China constrained by satellite observations: Implications for combustion and microbial sources, J. Geophys. Res., 112, D06301, https://doi.org/10.1029/2006jd007538, 2007.

Wittrock, F., Oetjen, H., Richter, A., Fietkau, S., Medeke, T., Rozanov, A., and Burrows, J. P.: MAX-DOAS measurements of atmospheric trace gases in Ny-Ålesund – Radiative transfer studies and their application, Atmos. Chem. Phys., 4, 955–966, https://doi.org/10.5194/acp-4-955-2004, 2004.

Wu, F., Xie, P., Li, A., Mou, F., Chen, H., Zhu, Y., Zhu, T., Liu, J., and Liu, W.: Investigations of temporal and spatial distribution of precursors SO$_2$ and NO$_2$ vertical columns in the North China Plain using mobile DOAS, Atmos. Chem. Phys., 18, 1535–1554, https://doi.org/10.5194/acp-18-1535-2018, 2018.

Zhang, Q., Streets, D. G., He, K., Wang, Y., Richter, A., Burrows, J. P., Uno, I., Jang, C. J., Chen, D., Yao, Z., and Lei, Y.: NO$_x$ emission trends for China, 1995–2004: The view from the ground and the view from space, J. Geophys. Res., 112, D22306, https://doi.org/10.1029/2007jd008684, 2007.

Zhang, Q., Streets, D. G., Carmichael, G. R., He, K. B., Huo, H., Kannari, A., Klimont, Z., Park, I. S., Reddy, S., Fu, J. S., Chen, D., Duan, L., Lei, Y., Wang, L. T., and Yao, Z. L.: Asian emissions in 2006 for the NASA INTEX-B mission, Atmos. Chem. Phys., 9, 5131–5153, https://doi.org/10.5194/acp-9-5131-2009, 2009.

Zhang, Q., Geng, G., Wang, S., Richter, A., and He, K.: Satellite remote sensing of changes in NO$_x$ emissions over China during 1996–2010, Chinese Science Bulletin, 57, 2857–2864, https://doi.org/10.1007/s11434-012-5015-4, 2012.

Zhang, X. Y., Sun, J. Y., Wang, Y. Q., Li, W. J., Zhang, Q., Wang, W. G., Quan, J. N., Cao, G. L., Wang, J. Z., Yang, Y. Q., and Zhang, Y. M.: Factors contributing to haze and fog in China, Chinese Sci. Bull., 58, 1178–1187, 2013.

Zhao, B., Wang, P., Ma, J. Z., Zhu, S., Pozzer, A., and Li, W.: A high-resolution emission inventory of primary pollutants for

the Huabei region, China, Atmos. Chem. Phys., 12, 481–501, https://doi.org/10.5194/acp-12-481-2012, 2012.

Zyrichidou, I., Koukouli, M. E., Balis, D., Markakis, K., Poupkou, A., Katragkou, E., Kioutsioukis, I., Melas, D., Boersma, K. F., and van Roozendael, M.: Identification of surface NO$_x$ emission sources on a regional scale using OMI NO$_2$, Atmos. Environ., 101, 82–93, https://doi.org/10.1016/j.atmosenv.2014.11.023, 2015.